Investigations of physical properties of the new EuMnCu$_2$P$_2$ compound

A. Jabar[a,b], S. Idrissi[c], and L. Bahmad[c,*]

[a] *LMHEP, Faculty of Sciences Aïn Chock, Hassan II University of Casablanca, B.P. 5366 Casablanca, Morocco,*
[b] *LPHE-MS, Science Faculty, Mohammed V University in Rabat, Morocco,*
[c] *Laboratory of Condensed Matter and Interdisciplinary Sciences, Faculty of Sciences, Mohammed V University,*
Av. Ibn Batouta, B.P. 1014 Rabat, Morocco,
[*] *e-mail: l.bahmad@um5r.ac.ma (L.B.)*

Received 7 December 2024; accepted 18 August 2025

This work explored the EuMnCu$_2$P$_2$ compound, examining its diverse physical properties, including structural, electronic, optical, and thermoelectric properties. The investigation used density functional theory (DFT) implemented in the Wien2k package. The GGA-PBE approach was employed to determine the exchange-correlation potential, with consideration for spin-orbit coupling (SOC). The results on structural properties of the EuMnCu$_2$P$_2$ compound indicate that the stable ground state of the compound is the ferromagnetic (FM) phase. Additionally, our electronic findings indicate the metallic behavior of the EuMnCu$_2$P$_2$ compound. We have examined several key parameters in assessing optical properties, such as electron energy loss, absorption coefficient, real and imaginary dielectric tensors, optical conductivity, refractive index, extinction coefficient and optical reflectivity. These properties provide valuable insights into how the material interacts with light and electromagnetic radiation. A significant finding in this study is that the compound exhibits exceptional absorption capabilities within the low and medium ultraviolet (UV) spectrums. This strong absorption in the UV region can be attributed to the material's unique electronic structure and response to the incident light. The excellent absorption properties make the compound a potential candidate for various applications in optoelectronics, photonic devices, and even solar energy conversion, where efficient utilization of UV light is crucial. Furthermore, we investigated the thermoelectric properties. Our findings reveal that the Seebeck coefficient decreases with increasing temperature, irrespective of the spin channel. The results suggest that the material displays an n-type behavior, as indicated by the negative values of the Seebeck coefficient. To gain a comprehensive understanding of the thermoelectric behavior of the alloy for practical applications.

Keywords: Tetragonal EuMnCu$_2$P$_2$ material; DFT method; seebeck coefficient; electron energy loss; thermoelectric properties.

DOI: https://doi.org/10.31349/RevMexFis.72.010502

1. Introduction

Interactions among electrons in strongly correlated systems significantly influence quantum particles' physical and magnetic properties, leading to the emergence of distinct phases of matter [1-3]. One intriguing scenario involves the competition and coexistence of superconductivity and magnetism, which typically exhibit mutual exclusion. However, in certain materials like cuprates [4] and heavy fermions [5], not only do magnetism and superconductivity coexist, but there is also a parallel interplay between the two in terms of energy dynamics [6]. Pnictide magnets with a 122-type stoichiometric configuration have become a unique platform for investigating the interplay between magnetism and superconductivity. Several pnictide materials, including BaFe$_2$As$_2$ and EuFe$_2$As$_2$, are recognized for showcasing unconventional superconductivity, with the underlying magnetism believed to play a crucial role in forming Cooper pairs [7-13]. Within the class of AFe$_2$As$_2$ compounds, where A represents divalent alkaline-earth or rare-earth metals, the manifestation of superconductivity is observed under specific conditions, such as chemical doping or external pressure application while adopting the tetragonal ThCr$_2$Si$_2$ ("122")-type structure [14-15]. For instance, EuCo$_2$As$_2$ undergoes a phase transition from a tetragonal phase to a collapsed tetragonal phase at 4.7 GPa [16]. Notably, recent investigations have revealed that applying pressure to the initially antiferromagnetic compound EuCo$_2$As$_2$ (TN = 47 K) induces a transition to ferromagnetism [17]. This change in magnetic ordering is linked to the stabilization of a mixed valence state of europium. Another study [18] demonstrated a substantial modification of antiferromagnetism in PrCo$_2$P$_2$ through aliovalent substitution within the Pr sub-lattice. Both Pr$_{0.8}$Eu$_{0.2}$Co$_2$P$_2$ and Pr$_{0.8}$Ca$_{0.2}$Co$_2$P$_2$ undergo a ferromagnetic phase transition, driven by the ordering of cobalt magnetic moments near 280 K. Additionally, EuCo$_2$P$_2$ and SrNi$_2$P$_2$ exhibit first-order phase transitions characterized by significant hysteresis and highly pronounced, anisotropic changes in lattice parameters at pressures of 30 kBar and 4 kBar, respectively [19]. Complex intermetallic structures are often described as intergrowth variants of simpler slabs with known structure types, such as elemental structures, binaries, or ternaries. Moreover, Examples of these structures include U$_3$Si$_2$ (with slabs related to W and AlB$_2$) [20,21], Mo$_2$FeB$_2$ (with CsCl and AlB$_2$ related slabs) [22], CeNiSi$_2$ (with BaAl$_4$ and AlB$_2$ related slabs) [23], and SmNiGe$_3$ (with slabs related to α-Po, BaAl$_4$, and AlB$_2$) [24]. Beyond the combination of slabs from binary compounds, the structural complexity can be significantly expanded by combining binary and ternary compounds. An illustrative instance is the platinum-rich silicide Sc$_4$Pt$_7$Si$_2$

[25], which represents an intergrowth variant of CsCl and TiNiSi-type slabs with compositions ScPt [26, 27] and ScPtSi [28, 29], both existing as separate compounds. Even more intricate are ternary structures that arise from two ternary slabs. Examples include the structure types $Y_2Rh_3Sn_5$ [30], $Yb_2Pt_3Sn_5$ [31], and $Ce_2Au_3In_5$ [32], all serving as intergrowth variants of TiNiSi and $NdRh_2Sn_4$-type slabs, as exemplified by the stannide $Sm_2Rh_3Sn_5$ [33]. In contrast to previously studied Heusler and perovskite-type materials, the $EuMnCu_2P_2$ compound exhibits distinct structural and physical properties, as highlighted in our earlier publications. In the present study, we further expand the analysis by incorporating optical reflectivity, extinction coefficient, and charge density evaluations-features that were not addressed in previous reports. These additions enhance the novelty of the work and offer deeper insight into the unique electronic and optical behavior of $EuMnCu_2P_2$. In this research paper, an in-depth exploration of the physical properties of the tetragonal $EuMnCu_2P_2$ alloy, based on rare earth elements, has been conducted utilizing the Density Functional Theory (DFT) method implemented through the Wien2k code. This investigation builds upon our recent studies of various materials using the same methodology [34-39]. The structure of the paper is organized as follows: In Sec. 2, we have presented the details of the computational approach adopted for the study. In Sec. 3, we have analyzed the outcomes obtained from the computational simulations. This section is further divided into sub-sections dedicated to the examination of structural, electronic, optical, and thermoelectric properties of the investigated materials. In Sec. 4, we summarize the key findings and insights derived from the study, highlighting the implications and potential applications of the results. It serves as a concluding section that encapsulates the research outcomes.

2. DFT approach

The structural, electronic, optical and thermoelectric properties of the $EuMnCu_2P_2$ compound are examined by the WIEN2K code [40]. This code is integrated into the FPLAPW (full potential linearized augmented plane wave) method composed of a set of subroutines [41]. The GGA-PBE (Perdew, Burke and Ernzerhof) approximation [42] was adopted to inspect the potential for exchange-correlation in the inputs to the FPLAPW approximation. The sizes of the basis sets are chosen by optimizing the parameter $\mathrm{RMT}\times\mathrm{K}_{\max}$, where RMT represents the smallest muffin tin radius in the unit cell, and $K_{\max}$ means the magnitude of the largest K vector in reciprocal space. In our study, the basic functions were fixed by the value $\mathrm{RMT}\times\mathrm{K}_{\max} = 9$. Thus, the integration of the Brillouin zone adopted the structure of the tetrahedron containing 1000 points. To treat Coulomb exchanges between electron-electrons in the elements Mn and Cu, the GGA+U approach was favored [43]. In this work, we denoted the effective parameter by $U_{\text{eff}} = U - J$, where U and J mean the Coulomb parameters and the exchange factor, respectively. To explore both the effect of spin-orbit coupling (SOC) and Hubbard potential (GGA+SOC+U), on the behavior of the magnetic and electronic characteristics of the compound $EuMnCu_2P_2$, we have chosen the values: $U_{\text{eff}} = 3.905$ eV for Mn and 6.476 eV for Cu, respectively. It should be noted that the self-consistent calculations only converge if the energy is lower than the threshold 10^{-5} Ry. Also, spin-orbit coupling (SOC) was added and approved such that the second variational approximation is consistent with scalar relativistic wave functions [44]. Concerning the modeling of the thermoelectric coefficients, we combined, in our calculations, both the modeling of the band structure as well as the Boltzmann transport approach including the rigid band approximation (RBA). In addition, the constant diffusion time approximation (CSTA) has been integrated into the BoltzTrap code [45]. The material $EuMnCu_2P_2$ is classified under space group P-3m1 number 164, exhibiting a body-centered tetragonal structure, as shown in Fig. 1. More details on the crystal arrangement of Eu, Mn, Cu and P atoms are grouped in Table I.

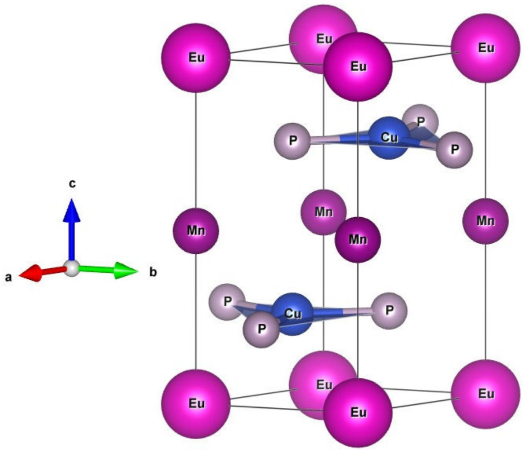

FIGURE 1. A sketch of the crystal structure of $EuMnCu_2P_2$.

TABLE I. Atomic Positions in the $EuMnCu_2P_2$ Material.

	x	y	z
Eu	0	0	0
Mn	0	0	0.5
Cu	0.66667	0.33333	0.25
Cu	0.33333	0.66667	0.75
P	0.66667	0.33333	0.75
P	0.33333	0.66667	0.25

3. Discussions and results

3.1. Lattice parameters and total energy

In this part, we carry out a structural study of the $EuMnCu_2P_2$ alloy. Structural optimization was carried out to optimize the lattice constants, mass modulus and static pressure transitions between the two phases: ferromagnetic (FM) and antiferro-

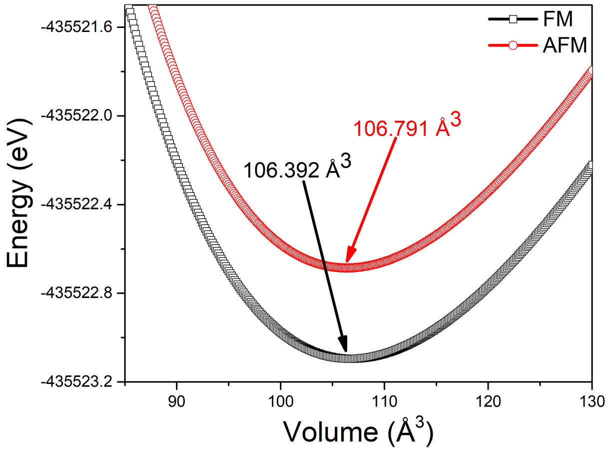

FIGURE 2. The variation of energy as a function of the volume of the EuMnCu$_2$P$_2$ compound.

TABLE II. Calculated equilibrium lattice parameters, such as the volume V_0(in Å^3), the bulk modulus B_0 (in GPa), its first pressure derivative B' and the minimum total energy E_0 (in eV) for the trigonal EuMnCu$_2$P$_2$ compound by applying the GGA+SOC+U approach.

	V_0 (Å^3)	B (GPa)	B'	E_0 (eV)
FM	106.791	78.853	4.440	-435523.095
AFM	106.392	79.239	4.674	-435522.686

magnetic (AFM). To optimize the equation of state we applied the empirical method of Birch-Murnaghan [46]. Indeed, the energy as a function of the volume of EuMnCu$_2$P$_2$ is presented in Fig. 2. The results obtained confirm the energy order of the phases: EFM $<$ EAFM, as predicted by the FP-LAPW approach. In addition, we optimized the EuMnCu$_2$P$_2$ material parameters, in the FM and AFM phases. These parameters are lattice constants ($a_0 = 4.139$ Å and $c_0 = 7.894$ Å), volume (V_0), volume modulus (B_0), first pressure derivative (B') and minimum total energy (E_0). The values calculated in this study are grouped in Table II. In particular, it is found that the FM phase is energetically more stable when compared to the AFM phase in the ground state phase of the EuMnCu$_2$P$_2$ material. To determine the most stable structure, the cohesive energy was calculated using the following formula:

$$E_{\text{Coh}} = \frac{\sum_x E_{\text{tot}}(x) - E_{\text{tot}}}{6}, \tag{1}$$

where E_{tot} is the total energy of the EuMnCu$_2$P$_2$ crystal, and $E_{\text{tot}(x)}$ represents the total energy of the isolated bulk elements x = Eu, Mn, Cu, and P. The calculated cohesive energy is 0.6915 eV/atom. Since E_{Coh} is positive, it indicates that the system is thermodynamically stable.

3.2. Electronic properties

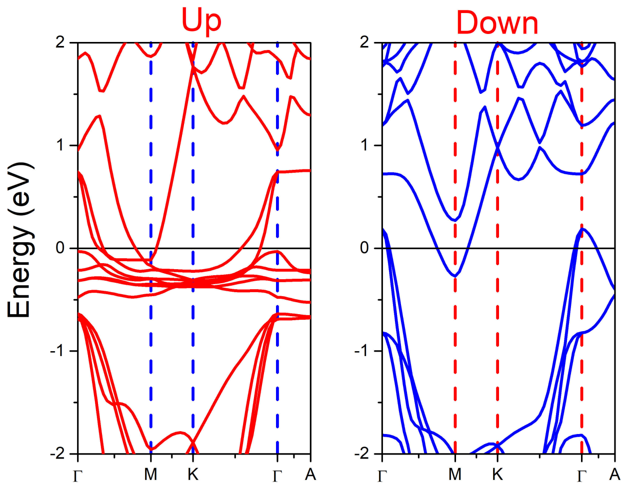

FIGURE 3. The band structure up and down of EuMnCu$_2$P$_2$ using GGA+SOC+U.

It should be noted that the studied compound EuMnCu$_2$P$_2$ is a new material. This study focuses on the examination of its electronic structure and bonding using density functional theory (DFT) calculations. Figure 3 represents the band structure of the compound EuMnCu$_2$P$_2$ as well as the high symmetry lines in the Brillouin zone, fitted by the 2 approaches: GGA-PBE and GGA + SOC + U, for the two spin directions (up and down). We focused on the first Brillouin zone, along the $\Gamma - M - K - \Gamma - A$ path. The results obtained show that the compound in question has metallic properties. This behavior is confirmed by the intersection of the Fermi level with the band structure of the material EuMnCu$_2$P$_2$. The electronic density of states (DOS) stands out as a crucial factor in delineating the electronic properties of this material. Utilizing the GGA-PBE and GGA+SOC+U methodologies, we have computed the total density of states (TDOS) and partial density of states (PDOS) for Eu, Mn, Cu, and P, as illustrated in Fig. 4. These diagrams not only disclose the participation of various atoms in the band structure but also highlight potential linear combinations. In the up valence bands, Eu

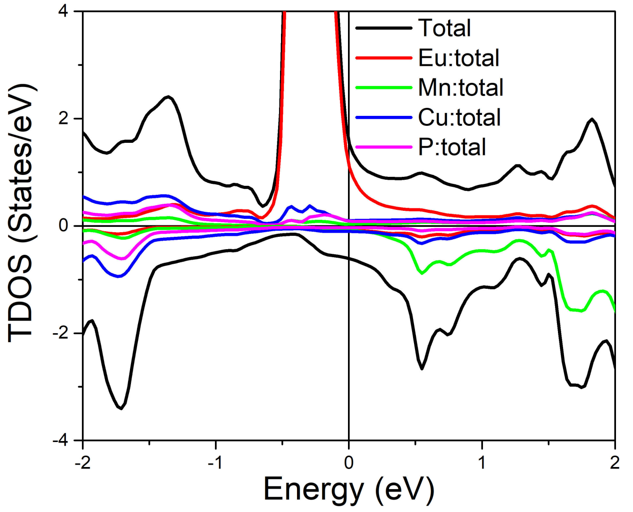

FIGURE 4. A schematic representation of the total density of states (TDOS) of EuMnCu$_2$P$_2$ using the GGA+SOC+U approach.

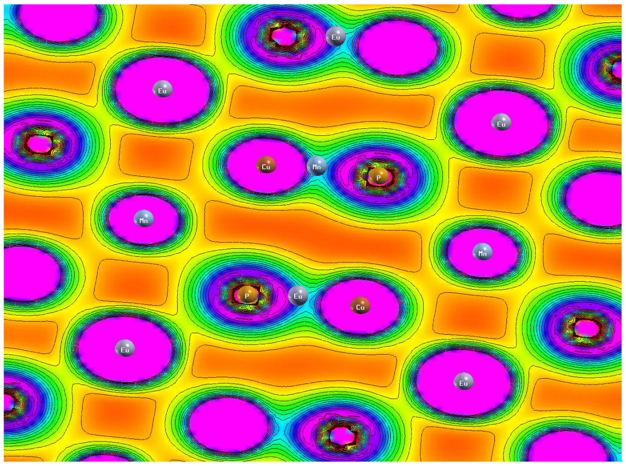

FIGURE 5. Electron localization function (ELF) maps for $EuMnCu_2P_2$.

states dominate, while Mn states predominate in the down conduction bands. Notably, Cu and P states significantly contribute not only to the valence band but also to the conduction band. The absence of a band gap, in line with the findings from the band structure, solidifies the metallic nature of the compound. Additionally, the magnetic nature of the compound is evident from the asymmetrical spin-up and spin-down contributions in TDOS. Figure 5 shows the Electron Localization Function (ELF) contour map for the $EuMnCu_2P_2$ compound in the (111) crystallographic plane. ELF values range from 0 (completely delocalized electrons) to 1 (fully localized electrons), with the color scale illustrating the degree of electron localization. The bright magenta and white regions (ELF $\approx$ 1) around the phosphorus (P) atoms indicate strong electron localization, characteristic of lone pairs or covalent bonding. The Cu-P and Mn-P bond regions exhibit intermediate ELF values (green to blue), suggesting partial covalent character due to shared electron density. In contrast, the regions around europium (Eu) atoms show low ELF values (orange to yellow), consistent with ionic behavior, where Eu acts as an electron donor with minimal electron localization. The observed asymmetry in the ELF distribution between Mn-P and Cu-P bonds reflects varying degrees of hybridization, with Mn-P bonds exhibiting more directional character, possibly indicating stronger covalent interactions. Overall, the ELF analysis reveals a mixed ionic-covalent bonding nature in $EuMnCu_2P_2$, with highly localized electrons near P atoms and weaker localization around Eu, offering insight into the compound's electronic and bonding characteristics.

3.3. Optical properties

In this section, we investigate the optical characteristics of the $EuMnCu_2P_2$ alloy, examining crucial aspects like absorption coefficient, electron energy loss, as well as the real and imaginary components of the dielectric tensor, optical conductivity, refractive index, extinction coefficient and optical reflectivity. Indeed, Figs. 6 illustrates these optical properties' results using the GGA+SOC+U approach. The absorption coefficient, a vital optical property, significantly impacts energetic materials and solar cells. It offers invaluable information on how extremely light of a specific wavelength and defined energy can enter a material before being captivated. This property is crucial for optimizing solar energy conversion efficiency. Since the sun emits light across diverse frequencies as photons, comprehending the absorption coefficient enables us to assess a material's capability to efficiently utilize solar energy. The depicted results in Fig. 6a) illustrate the behavior of the calculated absorption coefficient for $EuMnCu_2P_2$. The curves show an increase in intensity as the photon energies become higher, particularly in the ultraviolet (UV) domain. This observation holds for both the xx, yy, and zz directions. In physics, the absorption coefficient quantifies the extent to which a material absorbs light at different wavelengths. The increase in intensity with higher photon energies in the UV domain indicates that the material becomes more effective at absorbing light in this specific energy range. This behavior is noteworthy, as it provides insights into the material's response to varying photon energies and its potential applications, especially in the UV region. Moreover, the parameter called "electronic energy loss" of $EuMnCu_2P_2$ alloy was shown in Fig. 6b) in xx, yy and zz directions. It should be noted that the large values of the energy loss parameter are observed in the ultraviolet region. Also, peaks caused by inter-band transitions between various points of high symmetry were noted. Specifically, along the zz direction, the $EuMnCu_2P_2$ material exhibits the highest peak at the energy value of 0.4 eV, resulting from an energy loss function value of 12 eV. This finding suggests that the compound could serve as an effective absorber in the low and medium ultraviolet spectrum. Furthermore, the presence of a peak in the energy loss function confirms the dual nature, not only of the plasma resonance but also of the associated frequency called "plasma frequency". Beyond this plasma frequency value, the material exhibits metallic properties. The last distinctive peak constitutes crucial evidence, confirming the transition between the dielectric and metallic behaviors of the studied $EuMnCu_2P_2$ material. In addition, the calculation of dielectric constants is essential to the realization of efficient solar cells. This is required by their direct impact on the Coulomb interaction force between electron-hole pairs and charge carriers. They also make it possible to secure the ionic charges in the network of the material in question. In addition, the dielectric constant governs the magnitude of such interaction, significantly influencing processes like charge separation, transport, and recombination. It is well-known that solar cells can accomplish and control several interactions, resulting in better device performance and augmented energy conversion efficiency. The results are presented in Figs. 6c) and 6d), which correspond to the real and imaginary parts of the dielectric function along the xx, yy, and zz directions of the $EuMnCu_2P_2$ compound. The real part of the dielectric function, shown in Fig. 6c), displays an increasing trend up to certain peaks, followed by a decline to

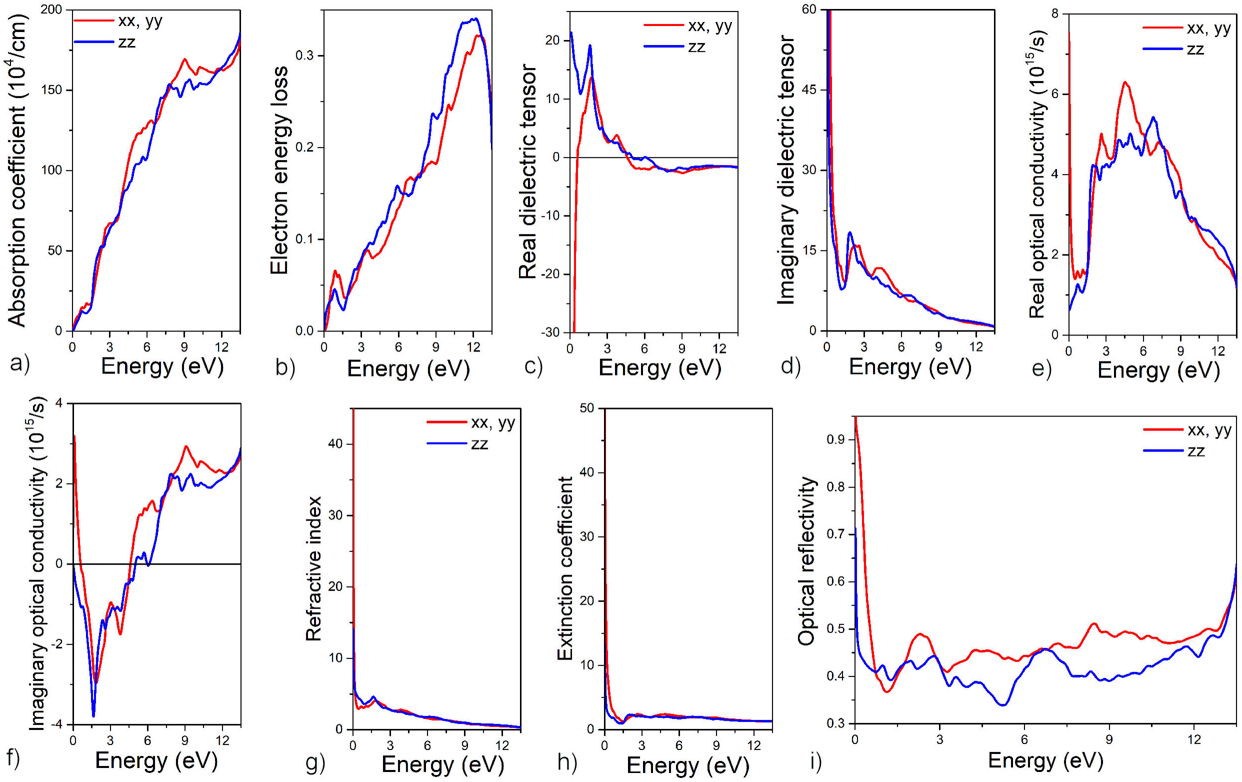

FIGURE 6. The energy dependency of the absorption coefficient a), the electron energy loss b), the real and imaginary part of dielectric tensor c) and d), the real and imaginary part of optical conductivity e) and f), the refractive index g), the extinction coefficient h), and the optical reflectivity (i) by using the GGA+SOC+U approach.

negative values as the photon energy increases. This behavior indicates that the material's response to an applied electric field is energy-dependent and affects how it interacts with different light frequencies. The static dielectric constant values, $\varepsilon_1(0)$, extracted from the real part of the dielectric function in all three crystallographic directions (xx, yy, and zz), provide insight into the material's polarizability in response to an external electric field. The imaginary part of the dielectric function, shown in Fig. 6d), reveals that light absorption predominantly occurs in the ultraviolet (UV) region, around 3 electron volts (eV). This indicates that the EuMnCu$_2$P$_2$ compound exhibits strong absorption in the UV range, highlighting its potential for applications in optoelectronic and photonic devices. The apparent divergence near 0 eV is a numerical artifact resulting from the Kramers-Kronig transformation or interpolation near the zero-energy limit. Such artifacts commonly appear in metallic systems, where intraband transitions dominate, particularly when a small but finite broadening parameter is assumed. For a given material, the optical conductivity constitutes a relationship between the magnitude of the inducing electric field and the current density obtained. Figures 6e), 6f) represents the real and imaginary parts, respectively, of the optical conductivity in the xx, yy and zz directions of the EuMnCu$_2$P$_2$ material. Regarding the real part shown in Fig. 6e), the peaks appear with increasing energy until reaching a maximum in the xx and yy directions. We used the GGA+SOC+U approach by considering the highest value 7×10^{15} s^{-1}. Then the plotted curves become a plateau, as the energy values increase. For the imaginary part, all curves show negative values at low energy. Then gradually increasing to reach positive values, for an energy close to the value 6 eV, see Fig. 6f). Figures 6g) and 6h) presents the calculated energy-dependent complex refractive index $N(\omega) = n(\omega) + ik(\omega)$ for the EuMnCu$_2$P$_2$ compound. Specifically, Fig. 6g) illustrates the real part of the refractive index $n(\omega)$, while Fig. 6h) displays the extinction coefficient $k(\omega)$, both plotted as functions of photon energy (in eV). These parameters are fundamental for understanding the interaction of the material with electromagnetic radiation, particularly its ability to refract and absorb light. The refractive index $n(\omega)$ describes the phase velocity of light in the material. A higher value of $n(\omega)$ indicates that light propagates more slowly through the material compared to a vacuum, signifying higher optical density and stronger light bending ability. At low photon energies (*e.g.*, near 0 eV), $n(\omega)$ corresponds to the static or low-frequency refractive index, which is essential for assessing the material response to static electric fields and long-wavelength radiation. Variations in $n(\omega)$ with increasing energy reflect optical dispersion. Sharp changes in $n(\omega)$ often coincide with strong electronic interactions, typically occurring near absorption edges or resonant transitions. Peaks in $n(\omega)$ just before the onset of absorption indicate enhanced material polarizability, while dips suggest regions of strong absorption. The extinction coefficient $k(\omega)$ quantifies the material's absorption of electromagnetic radiation. A higher $k(\omega)$ value indicates stronger attenuation of light as it penetrates the material. It is directly related to the imaginary part of the dielectric function and the absorption coefficient. The energy at which $k(\omega)$ begins to increase markedly defines the absorption edge of the material. For metallic materials, $k(\omega)$ remains non-zero even at low photon energies due to free carrier absorption. Peaks in the $k(\omega)$ spectrum correspond to strong interband or intraband transitions, where photon energy is sufficient to excite electrons. These absorption features are particularly relevant for evaluating the material's suitability for optoelectronic and light-harvesting applications. Regions with low $k(\omega)$ indicate transparency, while high values signify strong opacity and absorption. Fig. 6i) displays the calculated optical reflectivity $R(\omega)$ of EuMnCu2P2 as a function of photon energy. Reflectivity represents the fraction of incident light reflected from a material's surface and is key to understanding its optical behavior. For metallic compounds like $EuMnCu_2P_2$, reflectivity is high at low photon energies due to free-electron screening, consistent with the Drude model. As the energy increases, a sharp decline in reflectivity typically occurs near the plasma frequency, beyond which the material becomes more absorptive or transparent. Above this threshold, interband transitions generate characteristic peaks and valleys, corresponding to photon-induced electronic excitations. For $EuMnCu_2P_2$, these features-particularly in the UV range-highlight its strong light interaction and suggest promising applications in reflective coatings and optoelectronic devices.

3.4. Thermoelectric properties

Our investigations of the thermoelectric properties of the studied $EuMnCu_2P_2$ material have combined the electronic structure calculations with the Boltzmann transport theory [45]. To inspect the thermoelectric properties of the $EuMnCu_2P_2$ material, we used the BoltzTraP code. This code includes a part dedicated to band structure to calculate the parameters necessary for the estimation of thermoelectric properties using the constant relaxation time approach. It should be noted that this method underestimates the dependence of temperature in terms of the structure of energy bands. Also, the thermoelectric characteristic of the studied $EuMnCu_2P_2$ compound is assured by different physical parameters, such as:

- * the Seebeck coefficient (S),
- * the electrical conductivity (σ),
- * the electronic thermal conductivity (κ_{e}),
- * the lattice thermal conductivity (κ_{L}).

Here, we investigated the transport properties of $EuMnCu_2P_2$ by considering both spin-up and spin-down channels through the GGA+SOC+U approximation considering the temperature range [0, 600 K] (see Fig. 7). Through the integration of electronic structure calculations and Boltzmann transport theory, we can examine and forecast the thermoelectric performance of $EuMnCu_2P_2$, providing insights into its applicability for suitable thermoelectric applications. Utilizing the methods described in Ref. [47], we evaluated in our calculations the Seebeck coefficient given by:

$$S = \frac{S_\uparrow \sigma_\uparrow + S_\downarrow \sigma_\downarrow}{\sigma_\uparrow + \sigma_\downarrow}, \tag{2}$$

$$\sigma = \sigma_\uparrow + \sigma_\downarrow. \tag{3}$$

In Fig. 7a), the variation of the Seebeck coefficient (S) with temperature for $EuMnCu_2P_2$ alloy is depicted. Our findings reveal that the Seebeck coefficient decreases with increasing temperature, for the given spin channel. The latter finding confirmed the n-type behavior of the studied compound $EuMnCu_2P_2$. Moreover, this has been approved by negative values of the Seebeck coefficient. To understand the thermoelectric behavior of the $EuMnCu_2P_2$ alloy, it is necessary to calculate the total Seebeck coefficient of this compound. The behavior of this parameter is shown in Fig. 7a). Furthermore, the electrical conductivity divided by the relaxation time (σ/τ) is plotted as a function of temperature in Fig. 7b) for the $EuMnCu_2P_2$ material. We considered the two spin states (up and down) using the GGA + SOC + U approach. This approach accounts for the interaction between electrons and the effect of spin-orbit coupling, as well as the on-site Coulomb interaction (U). The graph demonstrates that the electrical conductivity divided by relaxation time (σ/τ) decreases with increasing temperature values for both spin states. This behavior implies that as the temperature increases, the material's ability to conduct electricity through the relaxation process. This could be due to the increased thermal energy disrupting the electronic structure or the balance between charge carriers and scattering mechanisms. Understanding these temperature-dependent electrical conductivity trends can help researchers develop strategies to optimize the material's performance in various applications, such as thermoelectric devices or spintronics. Initially, we compute the electronic thermal conductivity divided by relaxation time (κ_e/τ) for the total and both spin configurations as functions of temperature using the BoltzTraP package. In addition, we depicted in Fig. 7c) the behavior of electronic thermal conductivity (κ_e/τ) by relaxation time (τ) with temperature values belonging to the interval [0, 600 K]. The results visibly show an increase in electronic thermal conductivity with temperature, reaching the values: 33×10^{14} (W.m^{-1}.K^{-1}.s^{-1}), 18×10^{14} (W.m^{-1}.K^{-1}.s^{-1}) and 16×10^{14} (W.m^{-1}.K^{-1}.s^{-1}), for the total, spin-up, and spin-down, respectively, at 600 K. It is well-known that the lattice thermal conductivity, κ_L, is determined by computing the Debye temperature (θ_D) and the Grüneisen coefficient (γ) through calculations performed employing the Gibbs2 programs [48]. Additionally, the methodology integrates a

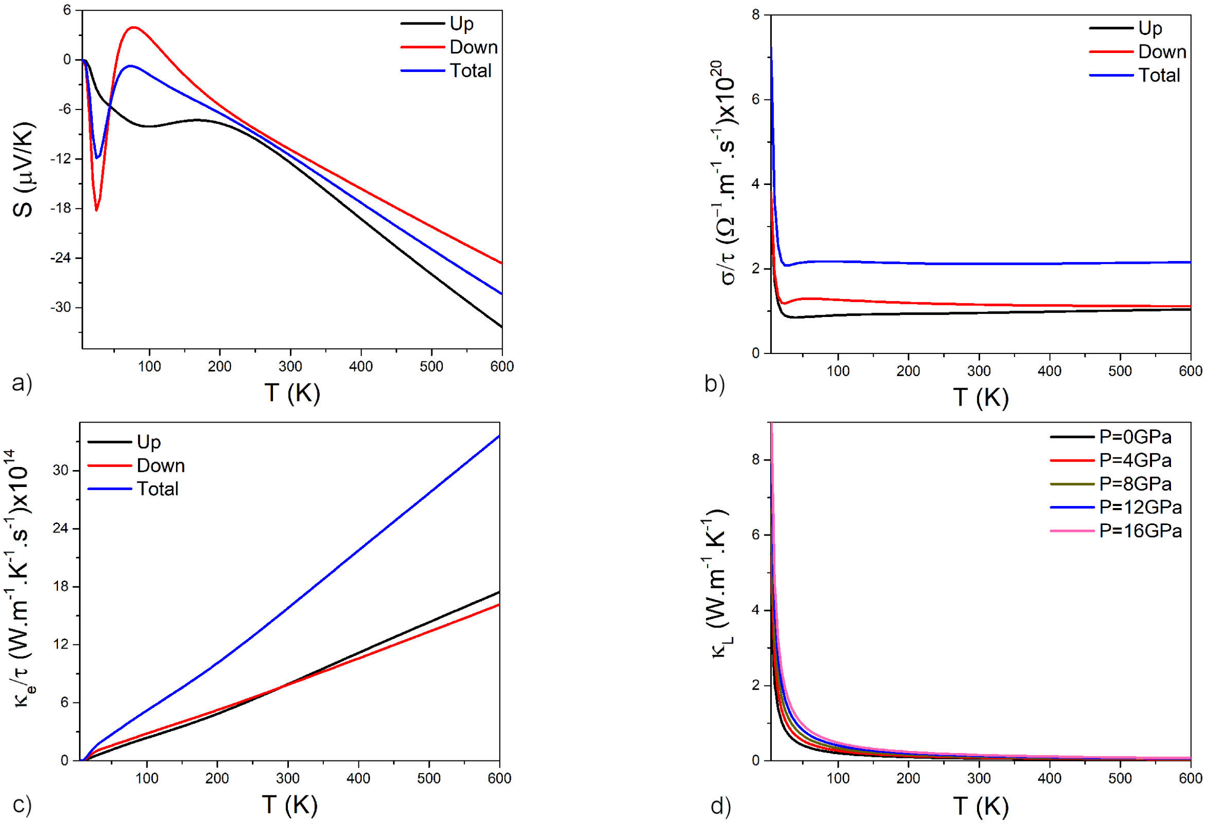

FIGURE 7. The Seebeck coefficient a), the electrical conductivity b), the electronic part of the thermal conductivity c), and the lattice part of the thermal conductivity d) of EuMnCu$_2$P$_2$ by using GGA+SOC+U approach.

unique relation to evaluate the lattice thermal conductivity (κ_L) employing the Slack approximation, given by the equation:

$$\kappa_L = \frac{A\,\theta_D^3 V^{1/3} M}{\gamma^2 n^{2/3} T}, \tag{4}$$

where A stands for a group of physical parameters. This parameter could be expressed as:

$$A = \frac{2.43 \times 10^{-8}}{1 - 0.514/\gamma + 0.228/\gamma^2}, \tag{5}$$

θ_D represents the Debye temperature, γ stands for the Grüneisen coefficient, V is the volume by atom, T denotes the temperature, n is the number of atoms in the primitive unit cell, and M represents the atomic mass. The lattice thermal conductivity (κ_L) of EuMnCu$_2$P$_2$ alloy, was calculated using the GGA-PBE approximations as described in Fig. 7d). It exhibits an exponential decrease with rising temperature and pressure. It is worth noting that the observed high value of κ_L signifies the presence of an anti-harmonic effect in the studied compound. The relatively low lattice thermal conductivity suggests that the material holds promise for thermoelectric applications.

4. Conclusions

In this work, we have explored the physical properties of the EuMnCu$_2$P$_2$ compound, including the structural, electrical, optical, and thermoelectric characteristics. Employing the Wien2k package and utilizing density functional theory (DFT), we conducted a comprehensive investigation. Our findings indicate that EuMnCu$_2$P$_2$ exhibits metallic behavior, and we established the ferromagnetic (FM) phase as its stable ground state. Additionally, we conducted a thorough analysis of the principal optical properties of this compound, such as the electron energy loss, the absorption coefficient, the real and imaginary parts of the dielectric tensors, the real and imaginary parts of the optical conductivity, the refractive index, extinction coefficient, and optical reflectivity. It is found that the studied compound exhibited exceptional absorption properties in the low and medium ultraviolet (UV) spectrum. The study delved into electronic conductivity, lattice thermal conductivity, electrical conductivity, and the Seebeck coefficient. The results revealed n-type behavior with a negative Seebeck coefficient, providing valuable insights into the distinctive characteristics of EuMnCu$_2$P$_2$.

Declaration of interest

The authors declare that they have no known competing financial interests or personal relationships that could have appeared to influence the work reported in this paper.

Data availability

All data generated or analyzed during this study are included in this published article.

Authors contribution statement

S. I. and L. B. conceived the presented idea and prepared figures. A. J. developed the theory and performed the computations. All authors contributed and discussed the results presented in the manuscript.

---

1. C. M. Varma, *Rev. Mod. Phys*. **48** (1976) 219.
2. P. Coleman and A. Schofield, *Nature* **433** (2005) 226.
3. S. Sachdev, Quantum Criticality, Cambridge Univ. (Press, New York, 1999).
4. J. M. Tranquada *et al*., *Nature* **429** (2004) 531.
5. P. Gegenwart, Q. Si and F. Steglich, *Nature Physics* **4** (2008) 186.
6. Z. Fisk *et al.*, *Science* **239** (1988) 33.
7. D.C. Johnston, *Adv. Phys.* **59** (2010) 803.
8. D.J. Scalapino, *Rev. Mod. Phys.* **84** (2012) 1383.
9. G.R. Stewart, *Rev. Mod. Phys.* **83** (2011) 1589.
10. A. Dahal *et al.*, *Phys. Rev. B* **99** (2019) 085135.
11. H. Hosono and K. Kuroki, *Physica C* **514** (2015) 399.
12. R.M. Fernandes, A. V. Chubukov, and J. Schmalian, *Nat. Phys*. **10** (2014) 97.
13. E. Dagotto, *Rev. Mod. Phys.* **85** (2013) 849.
14. J. Ballinger, L. E. Wenger, Y. K. Vohra, and A. S. Sefat, *Journal of Applied Physics* **111** (2012) 07E106.
15. R. Mahesh, T. Gnanapongothai, B. Rameshe, U. Reka, and B. Palanivel, Chemistry, Materials Science, (2014).
16. M. Bishop, W. Uhoya, G. Tsoi, Y. Vohra, A. Sefat, and B. Sales, *Journal of Physics. Condensed Matter: An Institute of Physics Journal*, **22** (2010) 425701.
17. X. Tan *et al.*, *J. Am. Chem. Soc.* **138** (2016) 2724.
18. K. Kovnir, W. M. Reiff, A. P. Menushenkov, A. A. Yaroslavtsev, R. V. Chernikov, and M. Shatruk, *Chem. Mater*. **23** (2011) 3021.
19. C. Huhnt, W. Schlabitz, A. Wurth, A. Mewis, and M. Reehuis, *Phys. Rev. B*, **56** (1997) 13796.
20. W. H. Zachariasen, *Acta Crystallogr*. **2** (1949) 94.
21. K. Remschnig, T. Le Bihan, H. Noël, P. Rogl, *J. Solid State Chem.* **97** (1992) 391.
22. W. Rieger, H. Nowotny, F. Benesovsky, *Monatsh. Chem.* **95** (1964) 1502.
23. O. I. Bodak, E. I. Gladyshevskii, *Sov. Phys. Crystallogr*. **14** (1970) 859.
24. O. I. Bodak *et al*., *Dopov. Akad. Nauk Ukr. RSR, Ser. B* **2** (1985) 36.
25. T. Harmening, L. van Wüllen, H. Eckert, U. Ch. Rodewald, R. Pöttgen, *Z. Anorg. Allg. Chem*. **636** (2010) 972.
26. A. T. Aldred, *Trans. Met. Soc. AIME* **224** (1962) 1082.
27. T. H. Geballe, B. T. Matthias, V. B. Compton, E. Corenzwit, G. W. Hull, L. D. Longinotti, *Phys. Rev*. **137** (1965) A119.
28. E. Hovestreydt, N. Engel, K. Klepp, B. Chabot, E. Parthé, *J. Less-Common Met*. **85** (1982) 247.
29. T. Harmening, H. Eckert, C. M. Fehse, C. P. Sebastian, R. Pöttgen, *J. Solid State Chem.* **184** (2011) 3303.
30. M. Meot-Meyer, G. Venturini, B. Malaman, J. Steinmetz, B. Roques, *Mater. Res. Bull*. **19** (1984) 1181.
31. R. Pöttgen, A. Lang, R.-D. Hoffmann, B. Künnen, G. Kotzyba, R. Müllmann, B. D. Mosel, C. Rosenhahn, *Z. Kristallogr.* **214** (1999) 143.
32. Ya. V. Galadzhun, R.-D. Hoffmann, R. Pöttgen, M. Adam, *J. Solid State Chem*. **148** (1999) 425.
33. B. Heying, J. Kösters, R.-D. Hoffmann, L. Heletta, R. Pöttgen, Z. *Naturforsch*, **72b** (2017) 753.
34. A. Jabar, S. Idrissi, L. Bahmad, *Solid State Communications*, **381** (2024) 115446.
35. S. Idrissi, A. Jabar, L. Bahmad, *International Journal of Quantum Chemistry*, **124** (2024) e27341.
36. H. Labrim, Y. Selmani, S. Ziti, S. Idrissi, R. El Bouayadi, D. Zejli, L. Bahmad, *Solid State Communications*, **363** (2023) 115105.
37. S. Idrissi, O. Mounkachi, L. Bahmad, A. Benyoussef, *Journal of the Korean Ceramic Society*, **60** (2023) 424.
38. S. Idrissi, H. Labrim, L. Bahmad, A. Benyoussef, *Ferroelectrics*, **606** (2023) 113.
39. S. Idrissi, *Integrated Ferroelectrics*, **225** (2022) 334.
40. P. Blaha, K. Schwarz, G.K.H. Madsen, D. Kvasnicka, J. Luitz, WIEN2k, An Augmented Plane Wave Plus Local Orbitals Program for Calculating Crystal Properties, Vienna University of Technology, Austria (2001).
41. O. K. Andersen, *Phys. Rev. B* **42** (1975) 3060.
42. J. P. Perdew, K. Burke and M. Ernzerhof, *Phys. Rev. Lett*. **77** (1996) 3865.
43. J. Camargo-Martínez and R. Baquero Parra, *Rev. Mex. Fi.*, **59** (2012).
44. W. Song, E. Zhao, J. Meng, and Z. Wu, *The Journal of Chemical Physics*, **130** (2009) 114707.
45. G. K. H. Madsen and D. J. Singh, *Computer Physics Communications*, **175** (2006) 67.
46. V. G. Tyuterev and N. Vast, *Computational Materials Science*, **38** (2006) 350.
47. H. J. Xiang and D. J. Singh, *Phys. Rev. B*, **76** (2007) 195111.
48. S. Yousuf and D. C. Gupta, *Materials Chemistry and Physics*, **192** (2017) 33.